American Mineralogist, Volume 108, pages 1612–1619, 2023

A high-pressure structural transition of norsethite-type $BaFe(CO_3)_2$: Comparison with $BaMg(CO_3)_2$ and $BaMn(CO_3)_2$

Chengcheng He[1,2,†], Chaoshuai Zhao[3], Jianjun Jiang[1], Pan Wang[1], and Heping Li[1,*,‡]

[1]Key Laboratory of High-temperature and High-pressure Study of the Earth's Interior, Institute of Geochemistry, Chinese Academy of Sciences, Guiyang, 550081, China
[2]University of Chinese Academy of Sciences, Beijing, 100049, China
[3]Center for High Pressure Science and Technology Advanced Research, Beijing 100193, China

Abstract

Investigations on the phase stability of the norsethite-type family [$BaMg(CO_3)_2$, $BaMn(CO_3)_2$, $BaFe(CO_3)_2$] under high-pressure conditions are of great significance for understanding the structure and metal cationic (Mg^{2+}, Fe^{2+}, Mn^{2+}) substitution mechanism in double divalent metal carbonates. The structural evolution and equation of state of $BaFe(CO_3)_2$ were studied at high pressure up to ~7.3 GPa by synchrotron X-ray diffraction (XRD) in diamond-anvil cell (DAC) in this study. $BaFe(CO_3)_2$ undergoes a reversible phase transition from $R\bar{3}m$ (α-phase) to $C2/c$ (γ-phase) space groups at ~3.0 GPa. The fitted elastic parameters are V_0 = 377.79(2) Å^3 and K_0 = 40.3(7) GPa for α-$BaFe(CO_3)_2$, V_0 = 483.24(5) Å^3 and K_0 = 91.2(24) GPa for γ-$BaFe(CO_3)_2$ using second-order Birch-Murnaghan equation of state (BM2-EoS). Besides, the vibrational properties and structural stability of complete norsethite-type minerals were also investigated first by Raman spectroscopy combined with DAC up to 11.1 GPa. Similar structural phase transitions occur in $BaMg(CO_3)_2$, $BaFe(CO_3)_2$, $BaMn(CO_3)_2$ at 2.2–2.6, 2.6–3.7, and 3.7–4.1 GPa, respectively. The onset phase transition pressures of the norsethite-type family are much lower than that of dolomite-type $Ca(Mg,Fe,Mn)(CO_3)_2$ and calcite-type $(Mg,Fe,Mn)CO_3$ carbonates. These results provide new insights into the divalent cation substitution effects on the stability and structural evolution of carbonates under high-pressure conditions.

Keywords: Norsethite-type minerals, synchrotron X-ray diffraction, Raman spectroscopy, phase transition, diamond anvil cell; Earth Analogs for Martian Geological Materials and Processes

Introduction

Norsethite [$BaMg(CO_3)_2$], which can be derived from dolomite [$CaMg(CO_3)_2$] by exchanging Ca with Ba (Lindner et al. 2017), has been studied extensively in recent years because of its rapid precipitation at ambient conditions compared with dolomite and magnesite ($MgCO_3$) (Hood et al. 1974; Lippmann 1967, 1973; Böttcher et al. 1997; Böttcher 2000; Schmidt et al. 2013; Pimentel and Pina 2014, 2016; Liu and Li 2020). Moreover, as a typical double carbonate, the formation conditions and the potential influence on the global carbon cycle are of great significance for carbonate geochemistry (Scheetz and White 1977; Effenberger and Zemann 1985; Böttcher et al. 1997; Schmidt et al. 2013; Effenberger et al. 2014; Pippinger et al. 2014; Zhuravlev and Atuchin 2020). The end-member of the norsethite-type family includes $BaMg(CO_3)_2$, $BaMn(CO_3)_2$, and $BaFe(CO_3)_2$ (Liang et al. 2021; Böttcher et al. 2022). All of them are typical layer structures with octahedra (MO_6, M = Mg, Fe, Mn) and polyhedra (BaO_{12}) located exactly one above the other, parallel to the [001] direction and separated by triangular CO_3 groups (Böttcher et al. 1997, 2012; Böttcher 2000; Pippinger et al. 2014; Liang et al. 2019, 2021), as shown in Figure 1a.

The natural samples of norsethite and Mn-bearing norsethite were found in natural environments (e.g., Costanzo et al. 2006; Zidarov et al. 2009), and the Mg and Mn end-members of norsethite [$BaMg(CO_3)_2$ and $BaMn(CO_3)_2$] were also synthesized under high-pressure-temperature (*P-T*) conditions (e.g., Böttcher et al. 2012; Lindner et al. 2017, 2018; Liang et al. 2019). However, ferroan norsethite [e.g., $BaFe(CO_3)_2$] was never reported until recently successfully synthesized at high *P-T* conditions (Liang et al. 2021). Norsethite-type minerals serve as a crystal chemical and geochemical analog for the dolomite-type minerals, which are regarded as one of the most prominent deep carbon carriers (Effenberger and Zemann 1985; Böttcher 2000; Binck et al. 2020; Liang et al. 2021). Although the stability of $BaMg(CO_3)_2$, $BaMn(CO_3)_2$ under high *P-T* conditions was extensively studied using different methods (e.g., XRD, Raman spectroscopy, density functional theory) (Scheetz and White 1977; Effenberger and Zemann 1985; Böttcher et al. 1997; Schmidt et al. 2013; Effenberger et al. 2014; Pippinger et al. 2014; Lindner et al. 2017; Liang et al. 2019; Zhuravlev and Atuchin 2020), whereas the high-pressure behavior of $BaFe(CO_3)_2$ is still unclear. Synchrotron XRD, combined with DAC is a well-known technique to in situ measure the structural evolution under high-pressure conditions (Liu et al. 2016; Fu et al. 2017), by which we can get some clues for possible existence conditions of ferroan norsethite from its high-pressure stability.

Partial cation substitution in carbonates is very common in natural samples, and the effects of substitution with various

* E-mail: liheping@mail.gyig.ac.cn.
† Orcid 0000-0001-9047-0820
‡ Special collection papers can be found online at http://www.minsocam.org/MSA/AmMin/special-collections.html.

0003-004X/23/0009–1612$05.00/DOI: https://doi.org/10.2138/am-2022-8722

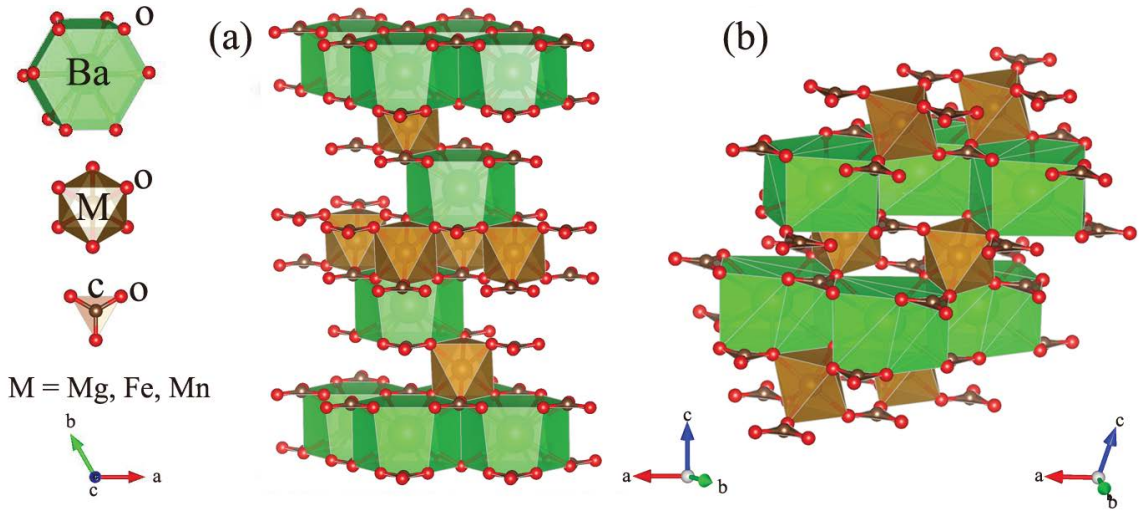

Figure 1. Crystal structures of α-$BaFe(CO_3)_2$ (**a**) and γ-$BaFe(CO_3)_2$ phase (**b**). (Color online.)

compositions and proportions on the physical and chemical properties of carbonates were extensively studied (e.g., Reeder and Dollase 1989; Lin et al. 2012; Palaich et al. 2015; Cerantola et al. 2015; Zhao et al. 2020; Gabitov et al. 2021). Mn^{2+} or Fe^{2+} cations can often be incorporated into the crystal structures in double carbonates, such as kutnahorite, ankerite, and norsethite-type $BaMn(CO_3)_2$ (Rividi et al. 2010; Efthimiopoulos et al. 2017; Wang et al. 2022). Previous studies showed that in the dolomite group, cation substitution of Mg^{2+} by Mn^{2+} could significantly lower the onset pressure of the phase transition (Wang et al. 2022), but this phenomenon was not obvious in the partial substitution of Mg^{2+} by Fe^{2+} (Mao et al. 2011; Merlini et al. 2012). So how about the influence of cation substitution in the norsethite-type minerals? There is still no answer yet. Raman spectroscopy has classically been used as a very effective and convenient tool to make semiquantitative estimates of solid solutions (e.g., Rividi et al. 2010; Farsang et al. 2018; Dong et al. 2019; Efthimiopoulos et al. 2019; Binck et al. 2020), which could be used to further study the mechanisms of Mg^{2+}, Fe^{2+}, Mn^{2+} replacement in the norsethite-type carbonates.

In this study, we first used in situ high-pressure XRD to characterize the structural changes of $BaFe(CO_3)_2$, calculated the isothermal compressibility, and compared it with other carbonate phases. Besides, the effects of metal cation radius on the high-pressure phase transition, Raman shifts, and pressure-induced mode shifts in the norsethite-type minerals were investigated by Raman spectroscopy. We also present the pressure dependence and mode Grüneisen parameters of Raman-active bands for $BaFe(CO_3)_2$, $BaMg(CO_3)_2$, and $BaMn(CO_3)_2$. These results provide new insights into the understanding of high-pressure behavior of the norsethite-type minerals.

Materials and methods

High-purity single-crystal of the norsethite-type minerals $BaFe(CO_3)_2$, $BaMg(CO_3)_2$, and $BaMn(CO_3)_2$ samples were synthesized at 3 GPa and 973 K for 2–12 h on a DS 6 × 600 t cubic anvil type apparatus. Norsethite-type crystals have a trigonal space group of $R\bar{3}m$, and no superstructure reflection was observed in the X-ray images. The lattice parameters were refined to be a = 5.022(1) Å, c = 16.752(1) Å, and V = 365.85(8) Å^3 for $BaMg(CO_3)_2$; a = 5.092(1) Å, c = 17.309(1) Å, and V = 388.69(8) Å^3 for $BaMn(CO_3)_2$; a = 5.062(1) Å, c = 17.027(1) Å, and V = 377.81(8) Å^3 for $BaFe(CO_3)_2$ at ambient conditions (Liang et al. 2021). A more detailed synthetic method and characterization of three samples can be referred to Liang et al. (2019, 2021).

High-pressure experiments for both synchrotron XRD and Raman spectroscopy were conducted by a symmetric type of DAC equipped with a pair of 400 μm culet-size diamond anvils. A thickness of 250 μm rhenium gasket was pre-indented to ~60 μm, and a diameter of around 160 μm was drilled by a laser drilling machine as the sample chamber. A volume ratio of 4:1 methanol and ethanol mixture was selected as the pressure transmitting medium (PTM), which can provide quasi-hydrostatic conditions up to ~10 GPa (Klotz et al. 2009). Several ruby (Cr^{3+}-doped α-Al_2O_3) spheres in Raman and gold (Au) powder in XRD experiments were loaded into the sample chamber for pressure calibration (Mao et al. 1986; Shen et al. 2020). The pressures and uncertainties were calculated by the measured pressure sensor before and after data collection.

For high-pressure, single-crystal Raman experiments, three double carbonates with good crystal morphology were loaded together into one sample chamber. Raman spectra were collected from 100 to 1200 cm^{-1} on a Renishaw 2000 micro-confocal laser Raman spectrometer with a 2400 lines/mm diffraction grating in the Key Laboratory of High-Temperature and High-Pressure Laboratory Institute of Geochemistry, Chinese Academy of Sciences, Guiyang. The Raman spectrometer was calibrated using a single-crystal silicon wafer at 520 cm^{-1} before experiments. Samples were excited by an argon ion laser (λ = 514.5 nm) operated at 20 mW with a focused laser spot of ~5 μm in diameter through an SLM Plan 50× Olympus microscope objective, and a spectrometer with a liquid nitrogen-cooled CCD detector was used to collect the Raman data. The accurate peak positions were fitted by the PeakFit software.

For high-pressure synchrotron powder-crystal XRD experiments, dozens of colorless and transparent single crystals of neutral $BaFe(CO_3)_2$ were picked out and ground with ethanol in an agate mortar for ~2 h to obtain homogeneous powder samples (Liang et al. 2021). To avoid powder scattering, powder samples were pressed slightly by two opposing diamond anvils to form a dense disk thinner than 20 μm. Subsequently, a small piece of dense sample was loaded into the DAC sample chamber. High-pressure synchrotron XRD experiments were carried out at the BL15U1 beamline of the Shanghai Synchrotron Radiation Facility (SSRF). The incident synchrotron X-ray beam was monochromatized to a wavelength of 0.6199 Å with a focused laser spot of ~2 × 3 μm^2 area. The diffraction patterns of the samples were collected by a MAR-165 charge-coupled device (CCD) detector. The distance of the sample-to-detector and the geometrical parameters of the detector were calibrated with cerium dioxide (CeO_2) powder. All 2D diffraction patterns collected were integrated into conventional 1D diffraction patterns by the Fit2D program as a function of 2θ (Hammersley et al. 1996). Diffraction data were collected at high pressures up to 7.3 GPa at intervals of 0.3–0.9 GPa. Whole XRD patterns were analyzed by the GSAS software package (Larson and Von Dreele 2000), and unit-cell parameters were refined by the Le Bail method (Le Bail et al. 1988).

Results and discussion

Equation of state of $BaFe(CO_3)_2$ at high pressure

The powder X-ray diffraction patterns of $BaFe(CO_3)_2$ with increasing pressure at room temperature are shown in Figure 2a. All the XRD peaks of $BaFe(CO_3)_2$ shift toward higher angles with increasing pressure below 2.8 GPa. Then the XRD patterns change significantly at 2.8 GPa, accompanied by the occurrence of several new peaks at ~8.5°, 9.1°, 14.3°, and 17° and the disappearance of peak at ~13°. These characteristics represent the onset phase transition of $BaFe(CO_3)_2$. Finally, the whole XRD peaks remain from 3.2 to 7.3 GPa.

The XRD patterns of $BaFe(CO_3)_2$ were analyzed by the Le Bail refinements using the GSAS program. Below 2.8 GPa, the XRD patterns agree well with the phase at ambient conditions (Liang et al. 2021), which yields a trigonal structure (space group $R\bar{3}m$) (Fig. 2b). Similar to α-norsethite [α-$BaMg(CO_3)_2$] (Pippinger et al. 2014), the trigonal phase is referred to as α-$BaFe(CO_3)_2$ in the following paragraphs. Above 3.2 GPa, the powder XRD patterns of the new phase are similar to γ-norsethite [γ-$BaMg(CO_3)_2$] with all the diffraction peaks indexed to the γ-$BaMg(CO_3)_2$-type structure, which yields a monoclinic structure (space group $C2/c$) (Pippinger et al. 2014). Two representative XRD patterns of α-$BaFe(CO_3)_2$ phase at 2.0 GPa and 300 K, and γ-$BaFe(CO_3)_2$ phase at 5.6 GPa and 300 K were exhibited in Figures 2b and 2c, respectively. The refinement results show great agreement with experimental values, which indicate the reliable structures of α- and γ-$BaFe(CO_3)_2$ phases. At 2.8 GPa, the existence of the characteristics of both α- and γ-$BaFe(CO_3)_2$ phases is noteworthy, indicating the coexistence of these two phases, namely, the mixture of α + γ-$BaFe(CO_3)_2$ phase.

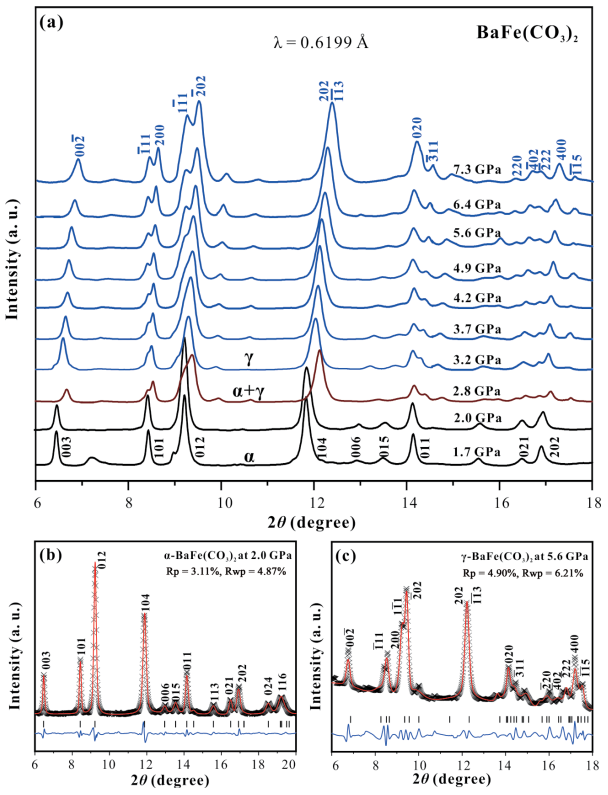

Figure 2. High-pressure XRD patterns of $BaFe(CO_3)_2$ (**a**), representative XRD patterns of α-$BaFe(CO_3)_2$ phase at 2.0 GPa and 300 K (**b**), and γ-$BaFe(CO_3)_2$ phase at 5.6 GPa and 300 K (**c**). The black, red, and blue solid lines represent the α-, α + γ- [coexistance of α-$BaFe(CO_3)_2$ and γ-$BaFe(CO_3)_2$ phase], and γ-$BaFe(CO_3)_2$. Le Bail profile fits of the structural model of $BaFe(CO_3)_2$ with: α-phase ($R\bar{3}m$) at 0–2 GPa and γ-phase ($C2/c$) at 3.2–7.3 GPa. The black forks, red solid lines, and blue lines stand for the observed, calculated, and deviation diffraction patterns, respectively. The short black lines are the standardized diffraction peak positions of α- and γ-$BaFe(CO_3)_2$ phase, respectively. (Color online.)

The pressure-volume (P-V) profiles of $BaFe(CO_3)_2$ are shown in Figure 3. The P-V profiles of α- and γ-$BaFe(CO_3)_2$ phases with the $R\bar{3}m$ and $C2/c$ structures were well fitted by a second-order Birch-Murnaghan equation of state (BM2-EoS) using the EoSFit7c software within the uncertainty of measurements (Birch 1947; Angel et al. 2014). The equation of BM-EoS was shown as follows:

$$P = \tfrac{3}{2}K_0[(V_0/V)^{7/3} - (V_0/V)^{5/3}] \times \{1 + \tfrac{3}{4}(K_0' - 4)[(V_0/V)^{2/3} - 1]\} \quad (1)$$

where V_0, V, K_0, and K_0' are the ambient-pressure unit-cell volume, high-pressure unit-cell volume, isothermal bulk modulus, and its pressure derivative ($K_0' = 4$) at ambient conditions. The fitting parameters are: V_0 = 377.79(2) Å^3 and K_0 = 40.3(7) GPa for α-$BaFe(CO_3)_2$, V_0 = 483.24(5) Å^3 and K_0 = 91.2(24) GPa for γ-$BaFe(CO_3)_2$. Compared to the norsethite-type family $BaMg(CO_3)_2$, the K_0 of α-$BaFe(CO_3)_2$ is distinctly smaller than that of α-$BaMg(CO_3)_2$ (K_0 = 66.2 GPa) (Pippinger et al. 2014). Different from the comparable K_0 values of dolomite-type carbonates, the K_0 values are 95(1), 92(1), and 85(6) for $CaMg(CO_3)_2$, $CaMg_{0.6}Fe_{0.4}(CO_3)_2$, and $Ca_{0.76}Mn_{1.24}(CO_3)_2$, respectively ($K_0' = 4$) (Merlini et al. 2017; Palaich et al. 2015). The difference may be attributed to the existence of superlattice in α-$BaMg(CO_3)_2$, which greatly improves its incompressibility (Helmersson et al. 1987; Pippinger et al. 2014; Dong et al. 2015).

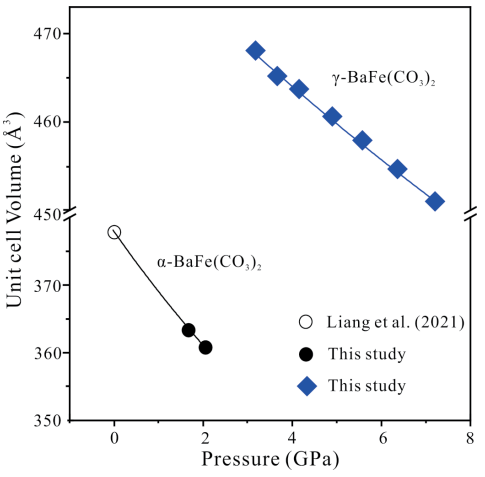

Figure 3. Pressure-volume profiles of $BaFe(CO_3)_2$. Black solid circles = α-$BaFe(CO_3)_2$ phase, this study; blue solid diamonds = γ-$BaFe(CO_3)_2$, this study; black open circle = α-$BaFe(CO_3)_2$ phase (Liang et al. 2021). Black and blue solid curves = the BM2-EoS fit of α-$BaFe(CO_3)_2$ and γ-$BaFe(CO_3)_2$, respectively. Error bars smaller than symbols are not shown for clarity. (Color online.)

The refined lattice parameters of $BaFe(CO_3)_2$ at various pressures were listed in Table 1. Changes in the unit cell volumes and lattice parameters throughout our pressure range are depicted in Figures 3–4. The length of the *a*- and *b*-axes contracted by 0.03(1) Å while the *c*-axis contracted gradually by 0.57(1) Å up to pressures near 2.0 GPa. Above 2.8 GPa, the length of the *c*-axis decreased by about 32% while that of *a*-axis increased by 72% (Fig. 4), which resulted in the expansion of the unit cell volume by about 30% (Fig. 3). For better comparison, we transform the parameter values of the α-phase to an equivalent monoclinic cell setting (Online Materials[1] Fig. S1). All lattice parameters and volume as a function of pressure clearly show discontinuous evolution, which can be assigned to the structural phase transition from α-phase to γ-phase. In addition, the compressibility of $BaFe(CO_3)_2$ becomes harder at high pressure, showing a nearly doubled bulk modulus K_0 of γ-$BaFe(CO_3)_2$. The calculated density of γ-$BaFe(CO_3)_2$ is also found to be 2% higher than the original phase at ambient conditions. Such a hardened behavior under high-pressure conditions is also found in other carbonates. The bulk moduli, K_0, are 92–95 and 76–83 GPa for dolomite-I, -II phases, respectively (Merlini et al. 2017). The values are 112 and 175 GPa for high- and low-spin states of siderite (Ming et al. 2012), 113 and 144 GPa for rhodochrosite $MnCO_3$-I and -II phases (Liu et al. 2016), 97 and 155 GPa for magnesite $MgCO_3$-I, -II phases, respectively (Maeda et al. 2017).

The axial compressibility and normalized lattice constants of $BaFe(CO_3)_2$ as a function of pressure at room temperature are shown in Figure 4d. For α-$BaFe(CO_3)_2$, our fitted axial modules to *a*, *b*, and *c* are $K_{a0} = K_{b0} = 324(22)$ GPa and $K_{c0} = 56(2)$ GPa, which indicate a remarkable compressional anisotropy with the compressibility of the *c*-axis being almost six times softer than that of other axes. The great compressional anisotropy can be attributed to the rigid unit of the CO_3 group, which is a coplanar arrangement and nearly parallel to the (0001) plane direction. As shown in Figure 1, the coplanar carbonate groups are out-of-plane tilt under high-pressure conditions (Pippinger et al. 2014), which results in the difference in the symmetries of the two phases and the decrease in compressional anisotropy for γ-$BaFe(CO_3)_2$ with $K_{a0} = 287(22)$ GPa, $K_{b0} = 504(72)$ GPa, and $K_{c0} = 207(16)$ GPa. The β angle steadily increases under compression within the

TABLE 1. Lattice constants and unit-cell volumes of the α-$BaFe(CO_3)_2$ and γ-$BaFe(CO_3)_2$ phase at high pressure and 300 K

Phase	*P* (GPa)	*a* (Å)	*b* (Å)	*c* (Å)	β (°)	*V* (Å³)	ρ (g/cm³)
α-phase	0[a]	5.062(1)	5.062(1)	17.027(1)	–	377.79(2)	3.34(1)
(*R*$\bar{3}$*m*)	1.7	5.037(1)	5.037(1)	16.540(1)	–	363.34(18)	3.47(2)
	2.0	5.032(2)	5.032(2)	16.456(1)	–	360.79(09)	3.50(1)
γ-phase	3.2	8.646(2)	5.030(1)	11.127(3)	104.742(2)	467.97(12)	3.59(4)
(*C*2/*c*)	3.7	8.619(2)	5.025(2)	11.104(3)	104.751(2)	465.06(14)	3.61(6)
	4.2	8.607(2)	5.025(2)	11.087(3)	104.791(2)	463.57(13)	3.63(1)
	4.9	8.589(2)	5.019(2)	11.048(3)	104.852(2)	460.33(14)	3.65(4)
	5.6	8.572(3)	5.015(3)	11.027(3)	105.023(3)	457.83(15)	3.67(3)
	6.4	8.561(3)	5.010(3)	10.981(3)	105.151(3)	454.55(15)	3.70(1)
	7.3	8.538(3)	4.993(3)	10.968(3)	105.341(3)	450.90(14)	3.73(1)

Notes: In α-phase, α = β = 90°, γ = 120°. In γ-phase, α = γ = 90°.
[a] Liang et al. (2021).

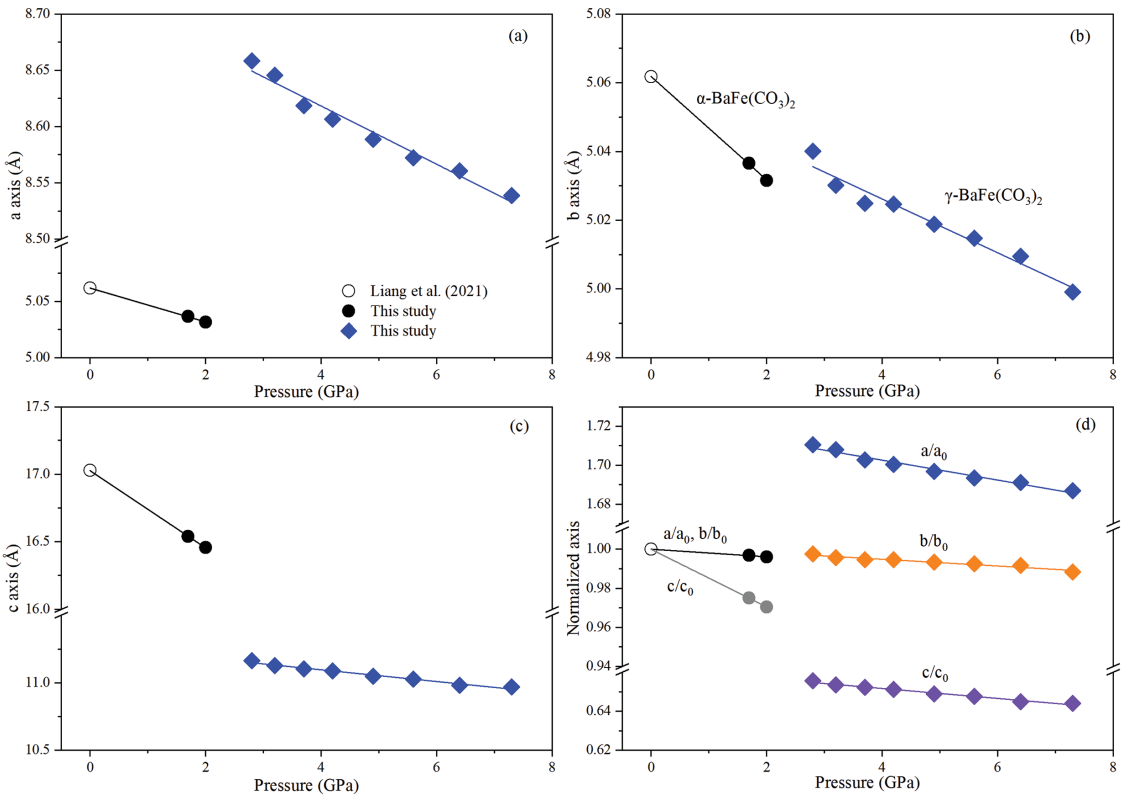

FIGURE 4. Second-order Birch-Murnaghan fits to the compression pressure-lattice parameters (**a**–**c**) and normalized lattice parameters (**d**) of $BaFe(CO_3)_2$. The black, blue, orange, and violet solid curves represent the BM2-EoS fittings of lattice parameters. Error bars smaller than symbols are not shown for clarity. (Color online.)

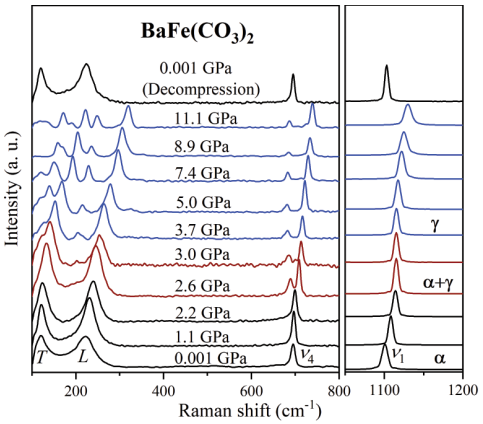

Figure 5. Representative Raman spectra of $BaFe(CO_3)_2$ at high pressures and room temperature. The black, red, and blue solid lines represent the α-, α + γ- [coexistance of α-$BaFe(CO_3)_2$ and γ-$BaFe(CO_3)_2$ phase], and γ-$BaFe(CO_3)_2$. The Raman spectrum of recovered sample (after decompression from 11.1 GPa) is consistent with that of α-$BaFe(CO_3)_2$ phase at ambient conditions, which indicates a reversible phase transition of $BaFe(CO_3)_2$. (Color online.)

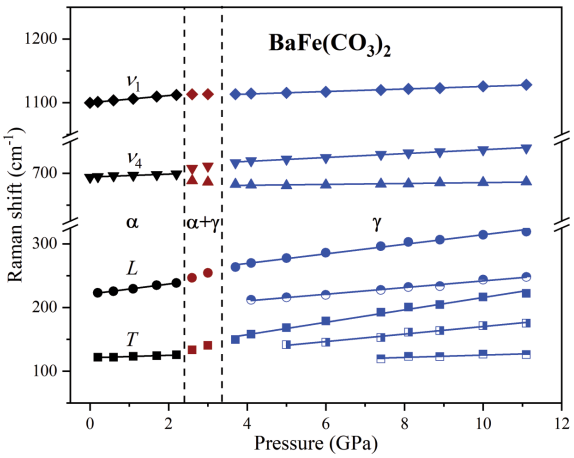

Figure 6. Representative Raman shifts of $BaFe(CO_3)_2$ at high pressures and room temperature. Error bars smaller than symbols are not shown for clarity. (Color online.)

pressure range (Online Materials[1] Fig. S1d). The *a*-axis shows a softening behavior at high pressure and the *b*- and *c*-axes show the opposite behavior.

Raman spectroscopy of the norsethite-type family [$BaFe(CO_3)_2$, $BaMg(CO_3)_2$, $BaMnCO_3)_2$] at high pressure

To better compare the high-pressure behaviors of $BaFe(CO_3)_2$, $BaMg(CO_3)_2$, $BaMn(CO_3)_2$, Raman spectra were obtained up to 11.1 GPa on the crystals of the complete norsethite-type family. The expansion of the vibration was obtained through factor-group analysis for norsethite-type crystals (Scheetz and White 1977; Zhuravlev and Atuchin 2020):

$$\tau_{tot} = 3A_{1g}(R) + 2A_{1u}(R) + A_{2g} + 5A_{2u}(IR) + 4E_g(R) + 6E_u(IR). \quad (2)$$

There are 7 Raman-active modes, which contain internal vibrations of the carbonate group and external lattice modes. The vibrations of the carbonate group (~700 to 1450 cm^{-1}) include fundamental symmetric and antisymmetric stretching (ν_1, ν_3), out-of-plane bending (ν_2), and in-plane bending (ν_4), among which ν_1 is the strongest characteristic peak. In addition, the external lattice modes (<400 cm^{-1}), derived mainly from the translational lattice mode *T* and librational lattice mode *L*, could also be obtained (Gillet et al. 1993). Similar Raman spectra of the norsethite-type family were observed in the wavenumber range from 100 to 1200 cm^{-1} at ambient conditions (Fig. 5; Online Materials[1] Figs. S2 and S4). A weak peak (ν_2) can be observed in the Raman spectrum of $BaMg(CO_3)_2$ at 880 cm^{-1}, which is not found in $BaMn(CO_3)_2$ and $BaFe(CO_3)_2$. The ν_2 internal mode belongs to the infrared-active mode, and chemical substitution affects its activity. Such a phenomenon was observed in the dolomite system (Gillet et al. 1993; Gunasekaran et al. 2006). Compared with previous studies of related Raman-active modes for the norsethite-type family, the slight differences in wavenumber for observed modes are due to the weak intensity, peak overlap, orientation dependence, and synthetic environment (Scheetz and White 1977; Schmidt et al. 2013; Liang et al. 2019, 2021).

The high-pressure Raman spectra of single-crystal of $BaFe(CO_3)_2$ were collected in the diamond window of 100–1200 cm^{-1} at ambient temperatures. The pressure dependence of the Raman spectra and shifts of $BaFe(CO_3)_2$ modes are shown in Figures 5 and 6. Obviously, with increasing pressure, all the Raman bands of $BaFe(CO_3)_2$ show blue shifts due to the decrease of corresponding bond length (Ba/Fe/C-O) caused by crystal compression. For pressures on $BaFe(CO_3)_2$ up to 2.6 GPa, the ν_4 mode splits into two individual components, then with further compression, *T* and *L* modes begin to split into two and three peaks, respectively, and no new peak occurs above 3.7 GPa. Meanwhile, the pressure-induced frequency shifts for the measurable modes all show a discontinuous evolution at 2.6 GPa, a transition area at 2.6 to 3.7 GPa, and a stable linear relation with pressure above 3.7 GPa. Referring to the XRD results of $BaFe(CO_3)_2$ in this study, both of these significant changes could be attributed to the occurrence of the structural phase transition from α-$BaFe(CO_3)_2$ to γ-$BaFe(CO_3)_2$. Combining the high-pressure results of XRD and Raman spectra, the more accurate phase transition range of $BaFe(CO_3)_2$ from α-phase to γ-phase should be 2.6 to 3.2 GPa, and the α-phase and γ-phase coexist in this pressure range. XRD results reveal that the CO_3 groups are out-of-plane tile at high pressures, which results in the vibrational environment change. The *T* mode spits into three peaks (*T*′, *T*″, *T*‴), and the pressure coefficient ($\partial\nu_i/\partial P$) changes from 2.03(11) to 1.89(5), 6.10(6), and 9.45(4) cm^{-1} GPa, respectively. The *L* mode splits into two modes (*L*′, *L*″) and the $\partial\nu_i/\partial P$ values decrease from 8.05(31) to 5.09(9) and 7.37(7) cm^{-1}/GPa, respectively. The ν_4 mode becomes two peaks (ν_4', ν_4'') with the $\partial\nu_i/\partial P$ from 2.48(9) cm^{-1}/GPa changing into 0.81(5) and 3.01(7) cm^{-1}/GPa, respectively. No split was observed in the ν_1 mode, but the pressure coefficient decreased from 5.71(2) to 2.04(3) cm^{-1}/GPa (Table 2).

The evolution and the pressure dependence of the Raman modes of $BaMg(CO_3)_2$ and $BaMn(CO_3)_2$ are shown in Online Materials[1] Figures S2–S5. From Raman spectra and shifts at high pressure, similar structural phase transitions can also be

TABLE 2. Vibrational parameters of $BaFe(CO_3)_2$ at high pressures and room temperature

Raman modes	α-$BaFe(CO_3)_2$ (0–2.2 GPa)			γ-$BaFe(CO_3)_2$ (3.7–11.1 GPa)		
	ν_{0i}	$d\nu_i/dP$	γ_i	ν_{0i}	$d\nu_i/dP$	γ_i
T	123	2.03(11)	0.68	107	1.89(5)	1.62
				111	6.10(6)	5.08
				118	9.45(4)	7.12
L	221	8.05(31)	1.51	189	5.09(9)	2.44
				239	7.37(7)	2.79
ν_4	694	2.48(9)	0.15	678	0.81(5)	0.11
				706	3.01(7)	0.39
ν_1	1100	5.71(2)	0.21	1106	2.04(3)	0.17

Notes: ν_{0i} are in cm^{-1}, $d\nu_i/dP$ are in cm^{-1}/GPa. The reference frequency at room pressure (ν_{i0}) and pressure coefficients, $\partial\nu_i/\partial P$, were used to calculate the mode Grüneisen parameters (γ_i) using the fitted K_{T0} values obtained in this study from BM2-EoS fitting: K_0 = 41.15(8) GPa for α-$BaFe(CO_3)_2$, K_0 = 91.4(19) GPa for γ-$BaFe(CO_3)_2$.

observed in $BaMg(CO_3)_2$ and $BaMn(CO_3)_2$ at 2.2–2.6 GPa and 3.7–4.1 GPa, respectively.

These results are comparable to previous high-pressure XRD and Raman experiments. Pippinger et al. (2014) reported that a structural transition occurred from an $R\bar{3}m$ to $C2/c$ structure at ~2.32 GPa in $BaMg(CO_3)_2$ by the single-crystal XRD experiments. Liang et al. (2019) found a similar structural phase transition may occur in $BaMn(CO_3)_2$ between 3.0 and 3.8 GPa by Raman scattering measurements. The slight difference in phase transition pressures may be attributed to the uncertainty of different detection methods.

When the pressures reach 2.6 and 4.1 GPa for the $BaMg(CO_3)_2$ and $BaMn(CO_3)_2$, respectively, the *T* and *L* modes undergo various degrees of splitting, with the values of the slope $\partial\nu_i/\partial P$ for each Raman vibration changing drastically. Meanwhile, the ν_4 mode splits into two new modes, and the slope $\partial\nu_i/\partial P$ of ν_1 mode exhibits an obvious decrease. The ν_2 mode of norsethite also shows a discontinuous change. The detailed pressure coefficients of $BaMg(CO_3)_2$ and $BaMn(CO_3)_2$ are listed in Online Materials[1] Tables S1 and S2, respectively. Reversibility of the phase transition of the norsethite-type minerals from α-phase to γ-phase has been confirmed by the consistency between decompressed spectra and initial spectra. In addition, the similar phase transition seems to complete faster in $BaMg(CO_3)_2$ and $BaMn(CO_3)_2$ than in $BaFe(CO_3)_2$, with no two-phase coexistence observed in the former two.

We calculate the isothermal mode Grüneisen γ_{iT} to further understand the elasticity properties of the norsethite-type minerals at high pressure, which is calculated as follows (Gillet et al. 1989):

$$\gamma_{iT} = (K_T/\nu_{i0})(\partial\nu_i/\partial P)_T \quad (3)$$

where ν_{i0} and $\partial\nu_i/\partial P$ are the frequencies fitted linearly by $\nu_i = \nu_{i0}+(\partial\nu_i/\partial P) \times P$, ν_{i0} is the frequency of mode ν_i at 0 GPa, and *P* is pressure. K_T is the bulk modulus with values of 40.3(7) and 91.2(24) GPa for α- and γ-$BaFe(CO_3)_2$ (this study), and 66.2(23) and 41.9(4) GPa for α- and γ-$BaMg(CO_3)_2$, respectively (Pippinger et al. 2014). The results are listed in Table 2 and Online Materials[1] Table S1. The average γ_{iT} values of CO_3 group [0.17 for $BaMg(CO_3)_2$, 0.18 for $BaFe(CO_3)_2$] are much smaller than that of the external lattice modes [1.685 for $BaMg(CO_3)_2$, 1.095 for $BaFe(CO_3)_2$] in the low-pressure phase. In the γ-phase, the difference of compressibility gets larger with a smaller γ_{iT} value of CO_3 group [0.06 for $BaMg(CO_3)_2$, 0.22 for $BaFe(CO_3)_2$], and a larger γ_{iT} value of the external lattice vibrations [2.09 for $BaMg(CO_3)_2$, 3.81 for $BaFe(CO_3)_2$]. The γ_{iT} values are small for the C-O bonds, which reflects their relative incompressibility and weak expansivity. Hence, the weaker bonds, corresponding to the external lattice modes at low frequency, are more affected by increasing pressure. The change in volume is mainly caused by the weaker bonds. It is obvious that the carbonate groups in $BaMg(CO_3)_2$ and $BaFe(CO_3)_2$ are much more incompressible than cation octahedra, which is consistent with other carbonates (e.g., $MgCO_3$ from Liang et al. 2018).

IMPLICATIONS

Cationic substitution is an important factor to affect the evolution and stability of crystal structure, phase transition pressure, and the positions and frequency shifts of spectroscopic peaks for different carbonate structures. The phase transition pressures of $BaMg(CO_3)_2$, $BaFe(CO_3)_2$, and $BaMn(CO_3)_2$ are 2.4(2), 2.7(5), and 3.9(2) GPa in this study, respectively. Compared with this study and previous results (Lin et al. 2012; Spivak et al. 2014; Cerantola et al. 2015; Merlini et al. 2015, 2017; Palaich et al. 2015; Fu et al. 2017; Vennari and Williams 2018; Binck et al. 2020; Chariton et al. 2020; Wang et al. 2022), the phase stability of norsethite-type $Ba(Mg,Fe,Mn)(CO_3)_2$, dolomite-type $Ca(Mg,Fe,Mn)(CO_3)_2$, and calcite-type $(Mg,Fe,Mn)CO_3$ carbonates at ambient temperature are presented in Figure 7. The effective cation radii of Ba^{2+}, Ca^{2+}, Mn^{2+}, Fe^{2+}, and Mg^{2+} are 1.35, 1.00, 0.83, 0.78, and 0.72 Å at ambient conditions, respectively (Shannon and Prewitt 1969). With the addition of the norsethite-type members, it is more clear that a smaller metal cation tends to stabilize the trigonal structure to

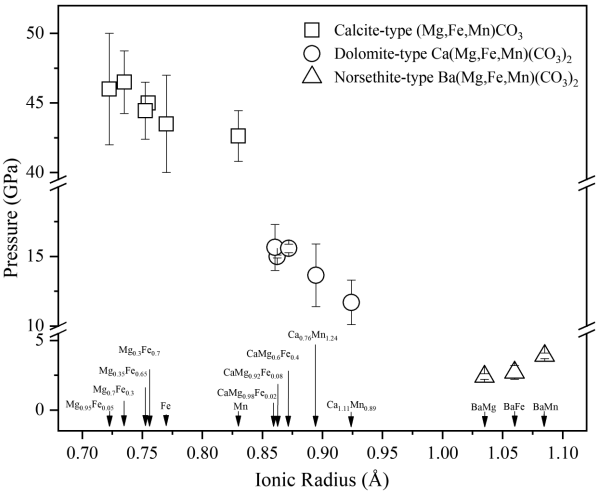

FIGURE 7. Phase stability of calcite-type $(Mg,Fe,Mn)CO_3$, dolomite-type $Ca(Mg,Fe,Mn)(CO_3)_2$, norsethite-type $Ba(Mg,Fe,Mn)(CO_3)_2$ carbonates at ambient temperature. The data are derived from this study for $BaMg(CO_3)_2$, $BaMn(CO_3)_2$, $BaFe(CO_3)_2$, for $Mg_{0.95}Fe_{0.05}CO_3$ from Spivak et al. (2014), for $Mg_{0.7}Fe_{0.3}CO_3$ from Chariton et al. (2020), for $Mg_{0.35}Fe_{0.65}CO_3$ from Fu et al. (2017), for $Mg_{0.3}Fe_{0.7}CO_3$ from Lin et al. (2012), for $FeCO_3$ from Cerantola et al. (2015), for $MnCO_3$ from Merlini et al. (2015), for $CaMg_{0.98}Fe_{0.02}(CO_3)_2$ from Binck et al. (2020), for $CaMg_{0.92}Fe_{0.08}(CO_3)_2$ from Vennari and Williams (2018), for $CaMg_{0.6}Fe_{0.4}(CO_3)_2$ from Merlini et al. (2017), for $Ca_{0.76}Mn_{1.24}(CO_3)_2$ from Palaich et al. (2015), and for $Ca_{1.11}Mn_{0.89}(CO_3)_2$ from Wang et al. (2022). The cation radii of Ba^{2+}, Ca^{2+}, Mn^{2+}, Fe^{2+}, and Mg^{2+} are 1.35, 1.00, 0.83, 0.78, and 0.72 Å, respectively (Shannon and Prewitt 1969).

higher pressure (Wang et al. 2022), and the phase transition pressures are much lower for norsethite-type carbonates than that of calcite- and dolomite-type carbonates. A cation octahedron with a smaller cation has shorter bonds and smaller compressibility; it thus can delay the polyhedral tilting and distortion at high pressure (Ross and Reeder 1992; Santillán and Williams 2004; Pippinger et al. 2014). However, different from the linear trend reported previously (Wang et al. 2015), the relationship tends to be nonlinear in the norsethite-type minerals. Taking a closer look at the effects of ionic radii on the phase transition of different carbonate structures, the substitution of Mg^{2+}, Fe^{2+}, and Mn^{2+} could change the kinetic barriers of phase transitions by changing the effective cation radii. The phase transition pressures increase with cation radius for norsethite-type minerals, while the results are opposite for both calcite- and dolomite-type carbonates. We attributed this to the structure difference in these crystals. In particular, the norsethite-type carbonates are composed of octahedral $(Mg,Fe,Mn)O_6$, trigonal planar $(CO_3)^{2-}$, and polyhedra BaO_{12} groups (Liang et al. 2019), while the dolomite-type carbonates are composed by alternating layers of octahedral $(Mg,Fe,Mn)O_6$ $(CO_3)^{2-}$, and octahedral CaO_6 groups (Binck et al. 2020). The ionic radii display a significant difference between $(Mg, Fe, Mn)^{2+}$ (0.72–0.83 Å) and Ba^{2+} (1.35 Å) in norsethite-type carbonates, while the values of $(Mg, Fe, Mn)^{2+}$ are close to Ca^{2+} (1.00 Å) in dolomite-type carbonates. Although the atomic distribution of the norsethite-type carbonates is topologically related to that of the dolomite-type minerals, the larger ratio between the radii of the $Ba^{2+}/(Mg^{2+}, Mn^{2+}, Fe^{2+})$ ions compared to that of $Ca^{2+}/(Mg^{2+}, Mn^{2+}, Fe^{2+})$ causes a distinct rotation of the carbonate group around (0001) plane (Liang et al. 2019). The difference in structure may lead to the change of high-pressure phase transition mechanism of cation $(Mg^{2+}, Mn^{2+}, Fe^{2+})$ substitution. These results provide new insights into the divalent cation substitution effects on the stability and structural evolution of carbonates under high-pressure conditions.

The effect of ionic radii on phase transition pressures has been found not only in carbonate minerals but also in other materials, such as rare-earth vanadates (Gong et al. 2018), gallium-bearing sphalerite-structure compounds (Zhang et al. 2021), and lead-free niobate ceramics (Yan et al. 2019). Consistent with the results in this study, the substance with a smaller ionic radius has a higher structural stability in isostructural materials. Once the relationship between the ionic radius and the phase transition pressure in a crystal structure is confirmed, the high-pressure structural stability of isostructural materials might be predicted. Moreover, the ionic radius can be added to the optimization variables to improve the high-pressure properties of the resistant materials (Yan et al. 2019), which may provide a possible way for high-pressure material synthesis and design.

Acknowledgments

We appreciate two anonymous reviewers for their constructive suggestions and comments, which helped improve the manuscript significantly. We thank Wen Liang for providing the norsethite samples and guidance on the experiments. We acknowledge Dawei Fan, Zhilin Ye, and Shijie Huang for the in situ X-ray diffraction measurements. We are also grateful for the support of beamline scientists at BL15U1 of SSRF.

Funding

This study was supported by the Strategic Priority Research Program (B) of the Chinese Academy of Sciences (XDB 18010401), the Chinese Academy of Sciences "Light of West China" Program (2019), and the National Natural Science Foundation of China (NSFC grant no. 42104101).

References cited

Angel, R.J., Alvaro, M., and Gonzales-Platas, J. (2014) EosFit7c and a Fortran module (library) for equation of state calculations. Zeitschrift für Kristallographie. Crystalline Materials, 229, 405–419, https://doi.org/10.1515/zkri-2013-1711.

Binck, J., Chariton, S., Stekiel, M., Bayarjargal, L., Morgenroth, W., Milman, V., Dubrovinsky, L., and Winkler, B. (2020) High-pressure, high-temperature phase stability of iron-poor dolomite and the structures of dolomite-IIIc and dolomite-V. Physics of the Earth and Planetary Interiors, 299, 106403, https://doi.org/10.1016/j.pepi.2019.106403.

Birch, F. (1947) Finite elastic strain of cubic crystals. Physical Review, 71, 809–824, https://doi.org/10.1103/PhysRev.71.809.

Böttcher, M.E. (2000) Stable isotope fractionation during experimental formation of Norsethite ($BaMg[CO_3]_2$): A Mineral Analog of Dolomite. Aquatic Geochemistry, 6, 201–212, https://doi.org/10.1023/A:1009646805933.

Böttcher, M.E., Gehlken, P.L., Skogby, H., and Reutel, C. (1997) The vibrational spectra of $BaMg(CO_3)_2$ (norsethite). Mineralogical Magazine, 61, 249–256, https://doi.org/10.1180/minmag.1997.061.405.08.

Böttcher, M.E., Effenberger, H.S., Gehlken, P.L., Grathoff, G.H., Schmidt, B.C., Geprägs, P., Bahlo, R., Dellwig, O., Leipe, T., Winde, V., and others. (2012) $BaMn[CO_3]_2$—A previously unrecognized double carbonate in low-temperature environments: Structural, spectroscopic, and textural tools for future identification. Chemie der Erde, 72, 85–89, https://doi.org/10.1016/j.chemer.2012.01.001.

Böttcher, M.E., Gehlken, P.L., and Liang, W. (2022) The mid-infrared spectrum of a new double carbonate, $BaFe[CO_3]_2$. Journal of Molecular Structure, 1250, 3–7, https://doi.org/10.1016/j.molstruc.2021.131899.

Cerantola, V., McCammon, C., Kupenko, I., Kantor, I., Marini, C., Wilke, M., Ismailova, L., Solopova, N., Chumakov, A., Pascarelli, S., and others. (2015) High-pressure spectroscopic study of siderite ($FeCO_3$) with a focus on spin crossover. American Mineralogist, 100, 2670–2681, https://doi.org/10.2138/am-2015-5319.

Chariton, S., McCammon, C., Vasiukov, D.M., Stekiel, M., Kantor, A., Cerantola, V., Kupenko, I., Fedotenko, T., Koemets, E., Hanfland, M., and others. (2020) Seismic detectability of carbonates in the deep Earth: A nuclear inelastic scattering study. American Mineralogist, 105, 325–332, https://doi.org/10.2138/am-2020-6901.

Costanzo, A., Moore, K.R., Wall, F., and Feely, M. (2006) Fluid inclusions in apatite from Jacupiranga calcite carbonatites: Evidence for a fluid-stratified carbonatite magma chamber. Lithos, 91, 208–228, https://doi.org/10.1016/j.lithos.2006.03.047.

Dong, X.C., Yue, J.L., Wang, E.Q., Li, M.L., and Li, G.Y. (2015) Microstructure and superhardness effect of VC/TiC superlattice films. Transactions of Nonferrous Metals Society of China, 25, 2581–2586, https://doi.org/10.1016/S1003-6326(15)63878-X (English ed.).

Dong, S., Berelson, W.M., Rollins, N.E., Subhas, A.V., Naviaux, J.D., Celestian, A.J., Liu, X., Turaga, N., Kemnitz, N.J., Byrne, R.H., and Adkins, J.F. (2019) Aragonite dissolution kinetics and calcite/aragonite ratios in sinking and suspended particles in the North Pacific. Earth and Planetary Science Letters, 515, 1–12.

Effenberger, H. and Zemann, J. (1985) Single crystal X-ray investigation of norsethite, $BaMg(CO_3)_2$: One more mineral with an aplanar carbonate group. Zeitschrift für Kristallographie, 171, 275–280.

Effenberger, H., Pippinger, T., Libowitzky, E., Lengauer, C.L., and Miletich, R. (2014) Synthetic norsethite, $BaMg(CO_3)_2$: Revised crystal structure, thermal behavior and displacive phase transition. Mineralogical Magazine, 78, 1589–1611, https://doi.org/10.1180/minmag.2014.078.7.05.

Efthimiopoulos, I., Jahn, S., Kuras, A., Schade, U., and Koch-Müller, M. (2017) Combined high-pressure and high-temperature vibrational studies of dolomite: Phase diagram and evidence of a new distorted modification. Physics and Chemistry of Minerals, 44, 465–476, https://doi.org/10.1007/s00269-017-0874-5.

Efthimiopoulos, I., Germer, M., Jahn, S., Harms, M., Reichmann, H.J., Speziale, S., Schade, U., Sieber, M., and Koch-Müller, M. (2019) Effects of hydrostaticity on the structural stability of carbonates at lower mantle pressures: The case study of dolomite. High Pressure Research, 39, 36–49, https://doi.org/10.1080/08957959.2018.1558223.

Farsang, S., Facq, S., and Redfern, S.A.T. (2018) Raman modes of carbonate minerals as pressure and temperature gauges up to 6 GPa and 500 °C. American Mineralogist, 103, 1988–1998.

Fu, S., Yang, J., and Lin, J.F. (2017) Abnormal Elasticity of single-crystal magnesiosiderite across the spin transition in Earth's lower mantle. Physical Review Letters, 118, 036402, https://doi.org/10.1103/PhysRevLett.118.036402.

Gabitov, R.I., Sadekov, A., Dyer, J., Perez-Huerta, A., Xu, H., and Migdisov, A. (2021) Sectoral and growth rate control on elemental uptake by individual calcite crystals. Chemical Geology, 585, 120589, https://doi.org/10.1016/j.chemgeo.2021.120589.

Gillet, P., Guyot, F., and Malezieux, J.M. (1989) High-pressure, high-temperature Raman spectroscopy of Ca_2GeO_4 (olivine form): Some insights on anharmonicity. Physics of the Earth and Planetary Interiors, 58, 141–154, https://doi.org/10.1016/0031-9201(89)90050-2.

Gillet, P., Biellmann, C., Reynard, B., and McMillan, P. (1993) Raman spectroscopic studies of carbonates part I: High-pressure and high-temperature behavior of calcite, magnesite, dolomite and aragonite. Physics and Chemistry of Minerals, 20, 1–18, https://doi.org/10.1007/BF00202245.

Gong, J., Fan, X., Dai, R., Wang, Z., Ding, Z., and Zhang, Z. (2018) High-pressure phase transition of micro- and nanoscale $HoVO_4$ and high-pressure phase diagram of $REVO_4$ with RE ionic radius. ACS Omega, 3, 18227–18233, https://doi.org/

10.1021/acsomega.8b02519.
Gunasekaran, S., Anbalagan, G., and Pandi, S. (2006) Raman and infrared spectra of carbonates of calcite structure. Journal of Raman Spectroscopy: JRS, 37, 892–899, https://doi.org/10.1002/jrs.1518.
Hammersley, A.P., Svensson, S.O., Hanfland, M., Fitch, A.N., and Hausermann, D. (1996) Two-dimensional detector software: From real detector to idealised image or two-theta scan. High Pressure Research, 14, 235–248, https://doi.org/10.1080/08957959608201408.
Helmersson, U., Todorova, S., Barnett, S.A., Sundgren, J.E., Markert, L.C., and Greene, J.E. (1987) Growth of single-crystal TiN/VN strained-layer superlattices with extremely high mechanical hardness. Journal of Applied Physics, 62, 481–484, https://doi.org/10.1063/1.339770.
Hood, W.C., Steidl, P.F., and Tschopp, D.G. (1974) Precipitation of norsethite at room temperature. American Mineralogist, 59, 471–474.
Klotz, S., Chervin, J.C., Munsch, P., and Le Marchand, G. (2009) Hydrostatic limits of 11 pressure transmitting media. Journal of Physics. D, Applied Physics, 42, 075413, https://doi.org/10.1088/0022-3727/42/7/075413.
Larson, A.C., and Von Dreele, R.B. (2000) GSAS general structure analysis system operation manual. Los Alamos Natl Lab LAUR 86-748, 179 p.
Le Bail, A., Duroy, H., and Fourquet, J.L. (1988) Ab initio structure determination of $LiSbWO_6$ by X-ray powder diffraction. Materials Research Bulletin, 23, 447–452, https://doi.org/10.1016/0025-5408(88)90019-0.
Liang, W., Li, Z., Yin, Y., Li, R., Chen, L., He, Y., Dong, H., Dai, L., and Li, H. (2018) Single crystal growth, characterization and high-pressure Raman spectroscopy of impurity-free magnesite ($MgCO_3$). Physics and Chemistry of Minerals, 45(5), 423–434.
Liang, W., Li, L., Yin, Y., Li, R., Li, Z., Liu, X., Zhao, C., Yang, S., Meng, Y., Li, Z., and others. (2019) Crystal structure of norsethite-type $BaMn(CO_3)_2$ and its pressure-induced transition investigated by Raman spectroscopy. Physics and Chemistry of Minerals, 46, 771–781, https://doi.org/10.1007/s00269-019-01038-w.
Liang, W., Peters, C., Li, L., Leupold, O., Li, H., and Böttcher, M.E. (2021) $BaFe[CO_3]_2$, a new double carbonate: Synthesis, structural characterization, and geostability implications for high and low *PT*. Chemie der Erde, 81, 125740, https://doi.org/10.1016/j.chemer.2021.125740.
Lin, J.F., Liu, J., Jacobs, C., and Prakapenka, V.B. (2012) Vibrational and elastic properties of ferromagnesite across the electronic spin-pairing transition of iron. American Mineralogist, 97, 583–591, https://doi.org/10.2138/am.2012.3961.
Lindner, M., Saldi, G.D., Jordan, G., and Schott, J. (2017) On the effect of aqueous barium on magnesite growth—A new route for the precipitation of the ordered anhydrous Mg-bearing double carbonate norsethite. Chemical Geology, 460, 93–105, https://doi.org/10.1016/j.chemgeo.2017.04.019.
Lindner, M., Saldi, G.D., Carrocci, S., Bénézeth, P., Schott, J., and Jordan, G. (2018) On the growth of anhydrous Mg-bearing carbonates—Implications from norsethite growth kinetics. Geochimica et Cosmochimica Acta, 238, 424–437, https://doi.org/10.1016/j.gca.2018.07.013.
Lippmann, F. (1967) Die kristallstruktur des norsethit, $BaMg(CO_3)_2$. Mineralogy and Petrology, 12, 299–318.
——— (1973) Sedimentary Carbonate Minerals, 229 p. Springer.
Liu, C. and Li, W. (2020) Transformation of amorphous precursor to crystalline carbonate: Insights from Mg isotopes in the dolomite-analogue mineral norsethite. Geochimica et Cosmochimica Acta, 272, 1–20, https://doi.org/10.1016/j.gca.2019.12.027. (BaMg(CO3)2)
Liu, J., Caracas, R., Fan, D., Bobocioiu, E., Zhang, D., and Mao, W.L. (2016) High-pressure compressibility and vibrational properties of $(Ca,Mn)CO_3$. American Mineralogist, 101, 2723–2730, https://doi.org/10.2138/am-2016-5742.
Maeda, F., Ohtani, E., Kamada, S., Sakamaki, T., Hirao, N., and Ohishi, Y. (2017) Diamond formation in the deep lower mantle: A high-pressure reaction of $MgCO_3$ and SiO_2. Scientific Reports, 7, 40602, https://doi.org/10.1038/srep40602.
Mao, H.K., Xu, J., and Bell, P.M. (1986) Calibration of the ruby pressure gauge to 800 kbar under quasi-hydrostatic conditions. Journal of Geophysical Research, 91 (B5), 4673, https://doi.org/10.1029/JB091iB05p04673.
Mao, Z., Armentrout, M., Rainey, E., Manning, C.E., Dera, P., Prakapenka, V.B., and Kavner, A. (2011) Dolomite III: A new candidate lower mantle carbonate. Geophysical Research Letters, 38, 2–5, https://doi.org/10.1029/2011GL049519.
Merlini, M., Crichton, W.A., Hanfland, M., Gemmi, M., Müller, H., Kupenko, I., and Dubrovinsky, L. (2012) Structures of dolomite at ultrahigh pressure and their influence on the deep carbon cycle. Proceedings of the National Academy of Sciences, 109, 13509–13514, https://doi.org/10.1073/pnas.1201336109.
Merlini, M., Hanfland, M., and Gemmi, M. (2015) The $MnCO_3$-II high-pressure polymorph of rhodocrosite. American Mineralogist, 100, 2625–2629, https://doi.org/10.2138/am-2015-5320.
Merlini, M., Cerantola, V., Gatta, G.D., Gemmi, M., Hanfland, M., Kupenko, I., Lotti, P., Müller, H., and Zhang, L. (2017) Dolomite-IV: Candidate structure for a carbonate in the Earth's lower mantle. American Mineralogist, 102, 1763–1766, https://doi.org/10.2138/am-2017-6161.
Ming, X., Wang, X.L., Du, F., Yin, J.W., Wang, C.Z., and Chen, G. (2012) First-principles study of pressure-induced magnetic transition in siderite $FeCO_3$. Journal of Alloys and Compounds, 510, L1–L4, https://doi.org/10.1016/j.jallcom.2011.08.079.
Palaich, S.E.M., Heffern, R.A., Watenphul, A., Knight, J., and Kavner, A. (2015) High-pressure compressibility and phase stability of Mn-dolomite (kutnohorite). American Mineralogist, 100, 2242–2245, https://doi.org/10.2138/am-2015-5095.
Pimentel, C. and Pina, C.M. (2014) The formation of the dolomite-analog norsethite: Reaction pathway and cation ordering. Geochimica et Cosmochimica Acta, 142, 217–223, https://doi.org/10.1016/j.gca.2014.07.021.
——— (2016) Reaction pathways toward the formation of dolomite-analogs at ambient conditions. Geochimica et Cosmochimica Acta, 178, 259–267, https://doi.org/10.1016/j.gca.2015.12.040.
Pippinger, T., Miletich, R., Effenberger, H., Hofer, G., Lotti, P., and Merlini, M. (2014) High-pressure polymorphism and structural transitions of norsethite, $BaMg(CO_3)_2$. Physics and Chemistry of Minerals, 41, 737–755, https://doi.org/10.1007/s00269-014-0687-8.
Reeder, R.J. and Dollase, W.A. (1989) Structural variation in the dolomite-ankerite solid-solution series: An X-ray, Mössbauer, and TEM study. American Mineralogist, 74, 1159–1167.
Rividi, N., van Zuilen, M., Philippot, P., Ménez, B., Godard, G., and Poidatz, E. (2010) Calibration of carbonate composition using micro-Raman analysis: Application to planetary surface exploration. Astrobiology, 10, 293–309, https://doi.org/10.1089/ast.2009.0388.
Ross, N.L. and Reeder, R.J. (1992) High-pressure structural study of dolomite and ankerite. American Mineralogist, 77, 412–421.
Santillán, J. and Williams, Q. (2004) A high-pressure infrared and X-ray study of $FeCO_3$ and $MnCO_3$: Comparison with $CaMg(CO_3)_2$-dolomite. Physics of the Earth and Planetary Interiors, 143-144, 291–304, https://doi.org/10.1016/j.pepi.2003.06.007.
Scheetz, B.E. and White, W.B. (1977) Vibrational spectra of the alkaline earth double carbonates. American Mineralogist, 62, 36–50.
Schmidt, B.C., Gehlken, P.L., and Böttcher, M.E. (2013) Vibrational spectra of $BaMn(CO_3)_2$ and a reanalysis of the Raman spectrum of $BaMg(CO_3)_2$. European Journal of Mineralogy, 25, 137–144, https://doi.org/10.1127/0935-1221/2013/0025-2272.
Shannon, R.D. and Prewitt, C.T. (1969) Effective ionic radii in oxides and fluorides. Acta Crystallographica. Section B, Structural Crystallography and Crystal Chemistry, 25, 925–946, https://doi.org/10.1107/S0567740869003220.
Shen, G., Wang, Y., Dewaele, A., Wu, C., Fratanduono, D.E., Eggert, J., Klotz, S., Dziubek, K.F., Loubeyre, P., Fat'yanov, O.V., and others. (2020) Toward an international practical pressure scale: A proposal for an IPPS ruby gauge (IPPS-Ruby2020). High Pressure Research, 40, 299–314, https://doi.org/10.1080/08957959.2020.1791107.
Spivak, A., Solopova, N., Cerantola, V., Bykova, E., Zakharchenko, E., Dubrovinsky, L., and Litvin, Y. (2014) Raman study of $MgCO_3$-$FeCO_3$ carbonate solid solution at high pressures up to 55 GPa. Physics and Chemistry of Minerals, 41, 633–638, https://doi.org/10.1007/s00269-014-0676-y.
Vennari, C.E. and Williams, Q. (2018) A novel carbon bonding environment in deep mantle high-pressure dolomite. American Mineralogist, 103, 171–174, https://doi.org/10.2138/am-2018-6270.
Wang, M., Liu, Q., Nie, S., Li, B., Wu, Y., Gao, J., Wei, X., and Wu, X. (2015) High-pressure phase transitions and compressibilities of aragonite-structure carbonates: $SrCO_3$ and $BaCO_3$. Physics and Chemistry of Minerals, 42, 517–527, https://doi.org/10.1007/s00269-015-0740-2.
Wang, F., Zhao, C., Xu, L., and Liu, J. (2022) Effects of hydrostaticity and Mn-substitution on dolomite stability at high pressure. American Mineralogist, 107, 2234–2241, https://doi.org/10.2138/am-2022-8248.
Yan, K., Wang, F., Chen, X., Wu, D., and Zhu, K. (2019) Effects of A-site ionic size on the phase transition behavior of lead-free niobate ceramics. Ceramics International, 45, 20323–20330, https://doi.org/10.1016/j.ceramint.2019.07.005.
Zhang, X., Dai, L., Hu, H., and Hong, M. (2021) Pressure-induced metallic phase transition in gallium arsenide up to 24.3 GPa under hydrostatic conditions. Modern Physics Letters B, 35, 1–12, https://doi.org/10.1142/S0217984921504601.
Zhao, C., Xu, L., Gui, W., and Liu, J. (2020) Phase stability and vibrational properties of iron-bearing carbonates at high pressure. Minerals (Basel), 10, 1–14, https://doi.org/10.3390/min10121142.
Zhuravlev, Y.N. and Atuchin, V.V. (2020) Comprehensive density functional theory studies of vibrational spectra of carbonates. Nanomaterials (Basel, Switzerland), 10, 1–19, https://doi.org/10.3390/nano10112275.
Zidarov, N., Petrov, O., Tarassov, M., Damyanov, Z., Tarassova, E., Petkova, V., Kalvachev, Y., and Zlatev, Z. (2009) Mn-rich norsethite from the Kremikovtsi ore deposit, Bulgaria. Neues Jahrbuch für Mineralogie. Abhandlungen, 186, 321–331, https://doi.org/10.1127/0077-7757/2009/0152.

Manuscript received July 21, 2022
Manuscript accepted October 27, 2022
Accepted manuscript online November 10, 2022
Manuscript handled by Ryosuke Sinmyo

Endnote:

[1]Deposit item AM-23-98722, Online Materials. Online Materials are free to all readers. Go online, via the table of contents or article view, and find the tab or link for supplemental materials.